metals

MDPI

Article

Corrosion Fatigue Characteristics of 316L Stainless Steel Fabricated by Laser Powder Bed Fusion

Balachander Gnanasekaran [1], Jie Song [2,3,*], Vijay Vasudevan [2,4] and Yao Fu [1,3,*]

[1] Department of Aerospace Engineering & Engineering Mechanics, University of Cincinnati, Cincinnati, OH 45221, USA; gnanasbr@mail.uc.edu
[2] Department of Mechanical and Materials Science Engineering, University of Cincinnati, Cincinnati, OH 45221, USA; vasudevk@ucmail.uc.edu
[3] Department of Aerospace and Ocean Engineering, Virginia Tech, Blacksburg, VA 24061, USA
[4] Department of Materials Science Engineering, University of North Texas, Denton, TX 76203, USA
* Correspondence: j.song.thu@gmail.com (J.S.); yaof@vt.edu (Y.F.)

Abstract: Laser powder bed fusion (LPBF) has been increasingly used in the fabrication of dense metallic structures. However, the corrosion related properties of LPBF alloys, in particular environment-assisted cracking, such as corrosion fatigue properties, are not well understood. In this study, the corrosion and corrosion fatigue characteristics of LPBF 316L stainless steels (SS) in 3.5 wt.% NaCl solution have been investigated using an electrochemical method, high cycle fatigue, and fatigue crack propagation testing. The LPBF 316L SSs demonstrated significantly improved corrosion properties compared to conventionally manufactured 316L, as reflected by the increased pitting and repassivation potentials, as well as retarded crack initiation. However, the printing parameters did not strongly affect the pitting potentials. LPBF samples also demonstrated enhanced capabilities of repassivation during the fatigue crack propagation. The unique microstructural features introduced during the printing process are discussed. The improved corrosion and corrosion fatigue properties are attributed to the presence of columnar/cellular subgrains formed by dislocation networks that serve as high diffusion paths to transport anti-corrosion elements.

Keywords: pitting corrosion; corrosion fatigue; dislocation network; laser powder bed fusion; 316L stainless steel

check for updates

Citation: Gnanasekaran, B.; Song, J.; Vasudevan, V.; Fu, Y. Corrosion Fatigue Characteristics of 316L Stainless Steel Fabricated by Laser Powder Bed Fusion. *Metals* **2021**, *11*, 1046. https://doi.org/10.3390/met11071046

Academic Editor: Gilbert Henaff

Received: 12 June 2021
Accepted: 23 June 2021
Published: 29 June 2021

Publisher's Note: MDPI stays neutral with regard to jurisdictional claims in published maps and institutional affiliations.

Copyright: © 2021 by the authors. Licensee MDPI, Basel, Switzerland. This article is an open access article distributed under the terms and conditions of the Creative Commons Attribution (CC BY) license (https://creativecommons.org/licenses/by/4.0/).

1. Introduction

Powder-based additive manufacturing (AM) techniques, such as laser powder bed fusion (LPBF) [1], are mostly used in the fabrication of dense metallic structures. The rapid solidification process and complex thermal cycles in AM can lead to unique microstructural features, defects, and residual stress that can result in properties drastically different from that of conventionally manufactured parts [2]. Although the microstructure and mechanical properties of alloys made from AM techniques have been studied extensively, there is a lack of deeper understanding regarding their corrosion related properties. The key microscopic characteristics in AM that affect the corrosion properties remain controversial [3–10]. The findings of the limited relevant studies regarding the effects of various types of microstructures/defects are briefly discussed in the following.

Nonequilibrium/atypical phase: Conventionally manufactured SSs contain MnS inclusions that typically reduce corrosion resistance. In LPBF alloys, nanoscale oxide inclusions (100 to 200 nm in diameter) enriched with Si, Al, and Mn were observed along the dislocation cell boundaries [11] instead of the MnS inclusions found in conventional ones. The LPBF alloys are reported to have enhanced pitting resistance due to the absence of MnS [5] in sodium chloride solution. However, in high temperature water, these oxide inclusions are reported to promote early initiation of microvoids and cause crack branching [12].

Columnar grains with strong directionality: Elongated grain structure along the build direction has been reported to have a detrimental impact and increase the stress corrosion

cracking (SCC) growth rates in high temperature water [13,14]. It is likely to be caused by the silica inclusions that are distributed along the grain boundaries, which preferentially dissolve and cause extensive crack branching.

Crystallographic texture: The strong crystallographic lamellar microstructure texture obtained by varying the scanning strategy has been found to result in the enhanced corrosion properties of SSs in sodium chloride solutions [15].

Cellular and columnar subgrain dislocation networks: These subgrain structures were reported to promote the formation of more compact and protective oxide film [6] and prevent deep penetration in localized corrosion [7], although no direct experimental evidence was provided.

Solute segregation: The solute-rich area (Si in Al alloys, Mo and Cr in 316L SS) and correspondingly depleted matrix lead to microgalvanic coupling and localized corrosion [16,17].

Residual stress: Reports of the effects of stress relief for residual stress in as-built 316L on corrosion behavior are mixed, with some studies reporting little or no significant changes in the corrosion properties during immersion testing [18], though a decrease in passive current and pitting potential was observed in cyclic potentiodynamic polarization (PP) [18]. Others have reported that the corrosion properties of heat-treated samples were slightly better [19]. However, it is worth mentioning that some of the stress relief treatments adopted in these studies can also lead to significant change in the subgrain cellular structure [20], which could very likely contribute to the measured corrosion properties.

Porosity: A systematic study of corrosion behavior as a function of the amount and size of pores in 316L has found that porosity in the range of 0.01% to 0.4% did not significantly affect the breakdown of passivity or critical pitting potential (E_{pitt}) in the PP curves, even though porosity is assumed as a possible site for the initiation of localized corrosion in AM parts. Instead, it has a more relevant effect on the metastable pitting and repassivation behavior [10].

Overall, there exist few studies on environment-assisted cracking behaviors such as the corrosion fatigue of AM alloys. Controversies remain regarding the effects of microstructural features on corrosion-related behaviors. Therefore, the main purpose of this work is to further understand pitting corrosion and corrosion fatigue properties, as well as the critical microstructural features that influence the corrosion related properties of AM metallic alloys. We have studied LPBF 316L SSs because it is of particular interest in marine, nuclear and biomedical applications. 316L possesses relatively superior ductility and excellent corrosion resistant properties over other materials. The pitting corrosion and corrosion fatigue properties in the sodium chloride (NaCl) solution will be focused on as SSs are well known to be susceptible to localized corrosion in chloride-containing solutions.

2. Materials and Methods

2.1. Materials

The AISI 316L stainless steel powders with a composition of Fe-17Cr-12Ni-3Mo (at%) supplied by PRAXAIR were utilized. Cubic samples were manufactured by an EOS M290 with a fixed laser diameter of 100 μm and an inert argon-purged atmosphere. The building direction was defined as the *Z*-axis (vertical direction), whereas the scanned layers were deposited on the horizontal plane (XY-plane). A bidirectional scanning strategy with a 67° rotation between layers was adopted. The layer thickness was fixed as 20 μm. The other processing parameters including laser power (P), scanning speed (v), and hatch space (H) were varied as shown in Table 1. The volumetric energy density was calculated via $E = P/(v \cdot t \cdot H)$ [21,22]. The laser power and hatch spacing were varied so that the volumetric energy density was changed correspondingly.

Table 1. The LPBF parameters used to manufacture the different specimens.

Sample	Power (P) W	Scan Speed (v) mm/s	Hatch Spacing (H) μm	Energy Density (E) J/mm^3
S1	150	1083.0	90	76.9
S2	195	1083.0	90	100.0
S3	240	1083.0	90	123.1
S4	150	1083.0	50	138.50
S5	195	1083.0	50	180.06
S6	240	1083.0	50	221.61
S7	195	1407.9	90	76.9

2.2. Electrochemical Corrosion Testing

To prepare working electrodes for the electrochemical tests, the specimens were sealed with an epoxy resin to expose an area of 0.32 cm^2, and ground to a P2400 grit finish. A three-electrode cell was employed with a graphite counter electrode and a saturated calomel reference electrode (SCE). All the potentials in the paper were given vs. the SCE electrode. The solution used in this investigation was 3.5 wt.% (0.61 M) NaCl (pH $\approx$ 5.8). The experiments were carried out under naturally aerated conditions at room temperature. Polarization curves were conducted at a sweep rate of 0.1667 mV/s, commencing from −150 mV (vs. open circuit potential (OCP)). The cyclic polarization curves were performed with the same forward scan rate at the same starting potential as the polarization test. Then, the scans were reversed back when the current density reached 0.5 mA/cm^2 at a reverse scan rate of 1.667 mV/s. The electrochemical measurements were recorded simultaneously using a potentiostat/galvanostat from Gamry. The measurements were repeated at least three times to confirm reproductivity and up to six tests were conducted for a few conditions for which the first three measurements showed poor reproductivity. The reported data was the average of at least three measurements.

2.3. Mechanical and Corrosion Fatigue Testing

The specimens for mechanical and high cycle corrosion fatigue tests were prepared following the ASTM E8 standard. The total length of the sample was 50 mm, and the gauge length was 15 mm. The width within the gauge length and that of the grip area were 3 mm and 11 mm, respectively. The thickness of the sample was 2 mm. The specimens for fatigue crack propagation analysis were prepared following the ASTM E647-15 standard. The length, width, and thickness were 35 mm, 10 mm, and 2 mm, respectively. The surface of the sample was ground to a P1200 grit finish so that the deteriorating surface roughness effect was avoided. The notch of 2.5 mm was machined using the wire-electrical discharge machining (EDM). The pre-crack extension of length around 1 mm from the machined notch was conducted in air or in NaCl solution (same as that used under crack growth measurement) at a ΔK = 20 MPa m$^{1/2}$. The crack length was measured in-situ using the direct current potential drop (DCPD) method. The calculation of crack length from the electrical potential difference across the crack followed Johnson's equation [23]. The load ratio and stress range were maintained throughout the test, and the ΔK correspondingly increased as the crack advanced. The high cycle corrosion fatigue and fatigue crack growth tests are highly reproducible and the reported data is the average of at least two measurements.

2.4. Microstructural Characterization

The microstructures of samples were examined by scanning electron microscopy (SEM) and electron backscatter diffraction (EBSD). The samples for SEM/EBSD were electropolished with a solution of 12.5 vol.% sulfuric acid and 87.5 vol.% methanol at a potential of 50 V at room temperature, and then electrolytically etched in a 10 vol.% saturated oxalic acid solution at 12 V for 90 s.

3. Results

3.1. Electrochemical Measurement

3.1.1. PP Test for Pitting Corrosion

The LPBF specimens were subject to the PP testing, and typical polarization plots for conventional and as-printed 316L SSs are shown in Figure 1. As the applied potential increased from the OCP or corrosion potential, there was an initial increase in current density and then, as the passive layer was being formed, the current density remained relatively stable with increasing potentials. At some higher potentials, pits started to form due to irregularities in the passive layer surface or an increasingly hostile environment locally. Some of these pits remained stable which led to an immediate increase in current density. This potential is the pitting potential (E_{pitt}), and the value of the E_{pitt} gives an insight into the ability of the material to resist stable pitting (Figure 1a).

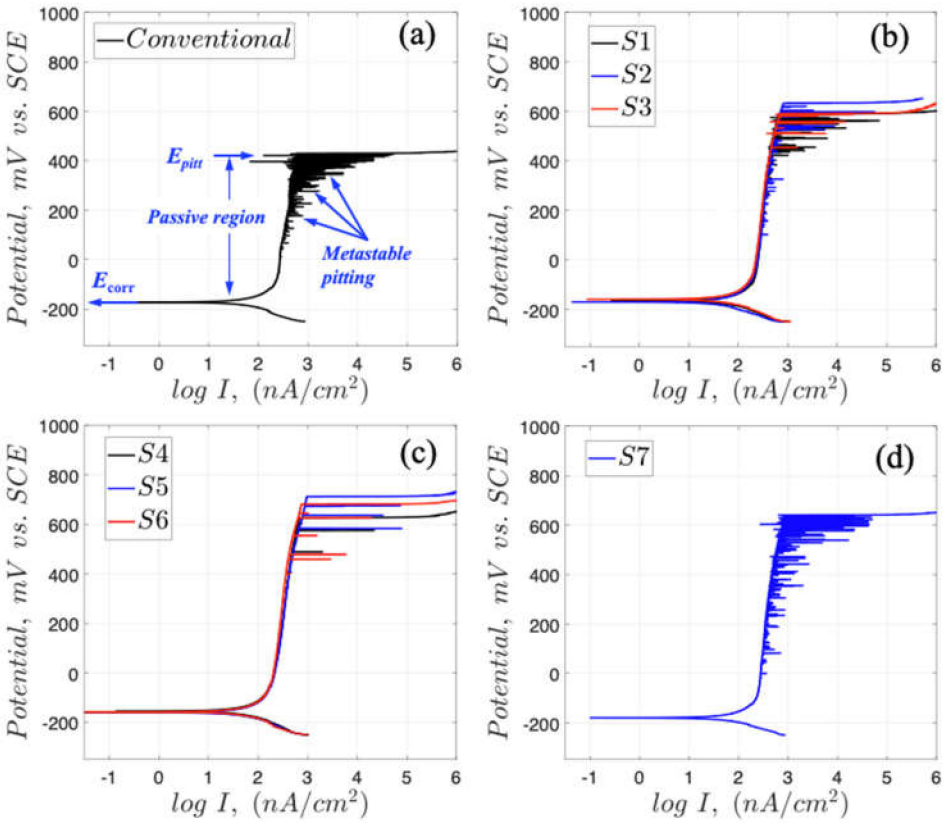

Figure 1. (**a**) Potentiodynamic polarization (PP) curves of the conventional sample, PP curves of the LPBF 316L SS at (**b**) H = 90 µm (S1–S3) and (**c**) H = 50 µm (S4–S6) with an increasing laser power from 150 W to 240 W; (**d**) PP curves of sample 7 not showing inferior corrosion property. Unless labeled otherwise, the electrochemical test was conducted on the XY plane (horizontal plane).

The PP curves reveal remarkably increased pitting potential (over 200 mV) of the LPBF 316L under certain chosen processing conditions, i.e., sample 5 (P = 195 W at H = 50 µm), compared to their conventional counterparts (Figure 1). Table 2 summarizes the values of the various parameters from the potentiodynamic curves for the different samples. Besides pitting potential, corrosion potential (E_{corr}) and corrosion current density (I_{corr}) were also extracted. The variation of E_{corr} and I_{corr} was insignificant within process parameters. Overall, LPBF 316L showed improved anti-corrosion properties compared to conventionally processed materials regardless of the varying laser power and hatch spacing. At both H = 50 µm and H = 90 µm, there was an initial small increase in E_{pitt}, followed by a small decrease. As the hatch spacing decreased, the pitting corrosion of

the sample increased by around 50–60 mV at the same laser power. Compared to a hatch spacing of 90 μm, metastable pitting events reduced in the case of H = 50 μm.

Table 2. Critical corrosion characteristics including corrosion potential E_{corr}, corrosion current density I_{corr}, and pitting potential E_{pitt}, extracted from the potentiodynamic polarization scan.

Sample Condition	150 W	195 W	240 W	150 W	195 W	240 W	Conventional
		90 μm			50 μm		
E_{corr}, mV vs. SCE	−159.6 ± 6.3	−165.4 ± 4.5	−151.6 ± 7.4	−154.9 ± 0.4	−163.2 ± 3.4	−164.4 ± 6.6	−164.0 ± 7.9
I_{corr}, nA/cm^2	27.9 ± 2.9	28.9 ± 11.7	28.3 ± 1.2	35.7 ± 4.2	37.7 ± 4.1	28.5 ± 3.4	24.9 ± 6.5
E_{pitt}, mV vs. SCE	635.5 ± 46.5	669.5 ± 36.5	639.5 ± 47.5	692.1 ± 65.2	744.5 ± 32.5	680.5 ± 0.5	458.0 ± 23.3

In order to understand the correlation between high porosity and the passivation and pitting of the LPBF 316L, the polarization behavior of sample 7, printed at relatively high speed, and thus containing a substantial number of pores (Figure S1 in the Supplementary Materials), was tested and is shown in Figure 1d. It was found that the pitting potential was around 641 mV, even higher than some dense samples. However, the metastable pitting events were more frequent. This is consistent with the finding in [10], where the critical pitting potential was not found to directly relate to the amount and size of pores in 316L, which affect metastable pitting instead.

3.1.2. Cyclic Polarization (CP) for Repassivation

The potentiodynamic polarization clearly demonstrates the significantly enhanced resistance to pitting corrosion as compared to the conventional samples, regardless of the hatch spacing and laser power. The most pronounced enhancement was found for sample 5 (P = 195 W at H = 50 μm). Therefore, we will be more focused on this printing condition in the following sections.

The CP measurements were conducted to further understand the repassivation and passive film properties. These tests were also carried out on the conventional samples for comparison. As shown in Figure 2, a positive hysteresis loop is observed related to the film degradation, largely due to localized corrosion. Furthermore, the lateral thickness of the hysteresis loop of all samples largely remains similar. This means that the conventional and LPBF samples have a similar rate of pitting. Repassivation potential is the potential at which the reverse scan rate crosses the forward scan rate. The difference between the pitting potential and repassivation potential, E_{pitt}-E_{repass}, indicates the repassivation characteristics of the surface. The higher the difference, the lower the propensity of the surface to repassivate. The repassivation potential for the LPBF-XY and XZ samples were 370.0 ± 20.1 and 410.0 ± 19.5 mV, respectively (Table 3). It was observed that the average repassivation potentials for the LPBF samples were higher than that for the conventional sample, which had a repassivation potential of 255.5 ± 33.6 mV. This means the LPBF samples repassivate quicker than conventional samples. Moreover, the difference between pitting and repassivation potential E_{pitt}-E_{repass} was also higher in conventional samples (297.4 ± 81.1 mV) than that in LPBF samples (225.2 ± 38.9 mV for LPBF-XZ and 257.5 ± 37.0 mV for LPBF-XY).

3.2. High Cycle Fatigue (HCF) and Fatigue Crack Propagation (FCP) in Air and 3.5 wt.% NaCl Solution

The samples printed at H = 50 μm and at P = 195 W, with their broad surface parallel to the XY plane, were subject to tensile and HCF testing with y as the loading direction (Figure 3). The pre-crack for FCP was formed on the XZ plane. The sample printed at the same laser power but at H = 90 μm was also investigated for comparison. The yield strength (YS) of the LPBF sample measured at an ambient temperature with a crosshead movement of 10 mm/min was 488 ± 10 MPa. This is significantly higher compared to the conventional sample, with YS = 388 ± 5 MPa, tested at the same condition (Figure 4a). The elongation at the fracture of the LPBF sample was reduced (15–17%) from the conventional

one (22–23%). Similar improvement in the yield strength and reduction in elongation of LPBF 316L samples compared to conventional ones has been reported in the past [2,15,24].

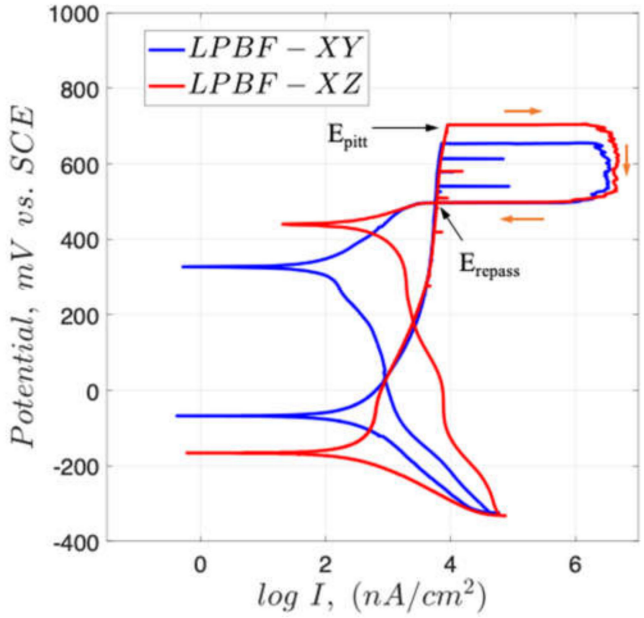

Figure 2. Cyclic polarization curves for multiple orientations of LPBF samples on different coordinate surfaces; orange arrows represent the direction of the hysteresis loop.

Table 3. Critical corrosion characteristics including repassivation potential E_{repass}, and the difference between the pitting potential and repassivation potential, E_{pitt}-E_{repass}, extracted from the CP scan.

	Conventional	LPBF-XY	LPBF-XZ
E_{repass}, mV vs. SCE	255.5 ± 33.6	370.0 ± 20.1	410.0 ± 19.5
E_{pitt}-E_{repass}, mV vs. SCE	297.4 ± 81.1	225.2 ± 38.9	257.5 ± 37.0

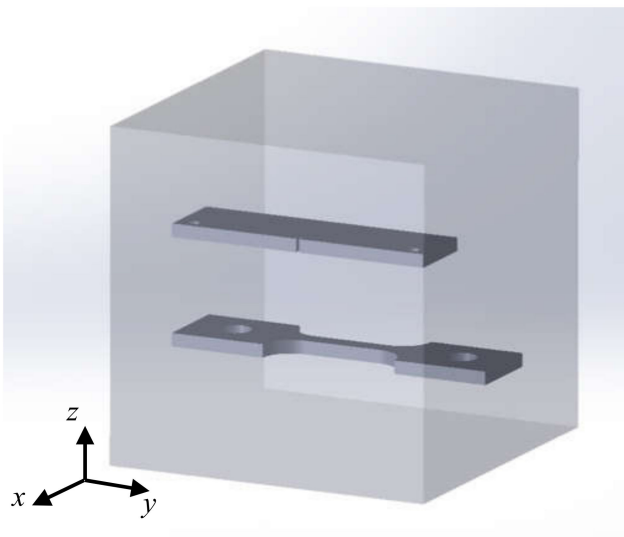

Figure 3. Sample orientation and its relationship with the build.

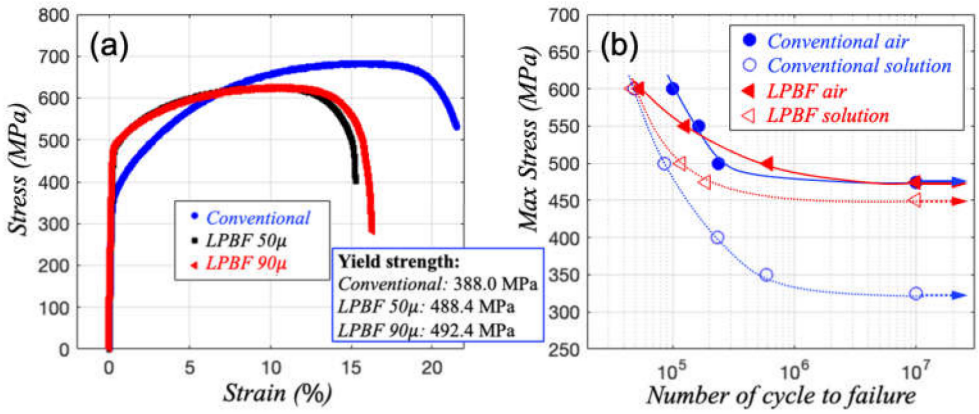

Figure 4. (**a**) Stress–strain relationship obtained through tensile loading test, and (**b**) high cycle fatigue life of smooth specimens of conventional and LPBF 316L SS printed at P = 195 W. Symbols with horizontal arrows in high cycle fatigue indicate that corrosion fatigue failure has not occurred after 10^7 load cycles.

High cycle fatigue life studies of the smooth samples of the conventional and LPBF 316L were conducted in air at room temperature at a frequency of 20 Hz. The cumulative fatigue damage in the form of S–N curves, i.e., the plot of stress vs. number of cycles to failure, is presented in Figure 4b. The load ratio R (= $\sigma_{min}/\sigma_{max}$) was fixed at 0.1, whereas the maximum applied external stress and the stress range ($\Delta\sigma = \sigma_{max} - \sigma_{min}$) were gradually reduced. However, the endurance limit, the stress range corresponding to the number of cycles of 10^7, was very close between the conventional and LPBF 316L in air (of around 475 MPa). Considering the fact that the yield strength of LPBF 316L was much higher than that of the conventional one, the comparable endurance limit between the two is very likely related to the presence of porosity in LPBF 316L. This endurance value is also close to that of the LPBF 316L reported in previous studies of around 500 MPa [24].

The high cycle fatigue tests were also conducted in the 3.5 wt.% NaCl solution under naturally aerated conditions. As shown in Figure 4b, the fatigue life of conventional 316L was greatly reduced, and a drastic decrease in the endurance limit σ_{ft} from 475 MPa to 325 MPa was found. In contrast, the change in the fatigue life of LPBF 316L from in air to in solution was limited. A reduction of only 25 MPa of the endurance limit was observed. Since crack initiation dominates the high cycle fatigue process, and in the corrosive environment a crack typically initiates from pitting sites, it is highly likely that the pitting sites which serve as the initial crack sites form faster in conventional, rather than LPBF, samples experiencing cyclic loading in the corrosive environment.

The fatigue crack propagation (FCP) in air and in solution were further tested and presented in Figures 5 and 6 to characterize the rate of crack advance per cycle (da/dN). The samples had the same broad surface as those for HCF tests, and the pre-crack surface ran parallel to the XZ plane (Figure 3). Here $\Delta K = K\Delta\sigma\sqrt{\pi a}$, where K is geometrically constant and a is the crack length. Comparing the conventional and LPBF samples (H = 90 and 50 μm) at R = 0.1 (Figure 5), the difference in the crack growth rate is quite significant. In air, the growth rates were higher in general in LPBF samples than conventional ones. In solutions at 20 Hz, the growth rate in conventional samples was lower at the early stage of crack growth (i.e., lower ΔK), but became higher as the crack grew further. Decreasing the loading frequency generally increases the deteriorative effects of the corrosive environment, so the tests were conducted at 2 Hz. It was found that the crack growth in the later stages was significantly higher for conventional samples.

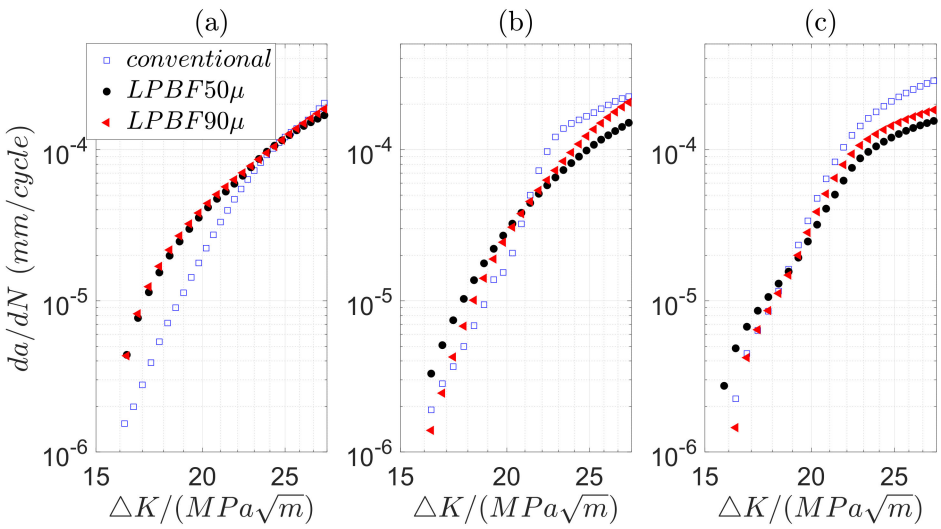

Figure 5. Fatigue crack growth kinetics of 316L SS at different corrosion fatigue parameters for conventional (labeled as conventional) and two LPBF samples at H = 90 µm and H = 50 µm (la-beled as LPBF90µ and LPBF50µ, respectively) at R = 0.1 in (**a**) air, (**b**) 3.5 wt.% NaCl solution at 20 Hz and (**c**) 3.5 wt % NaCl solution at 2 Hz.

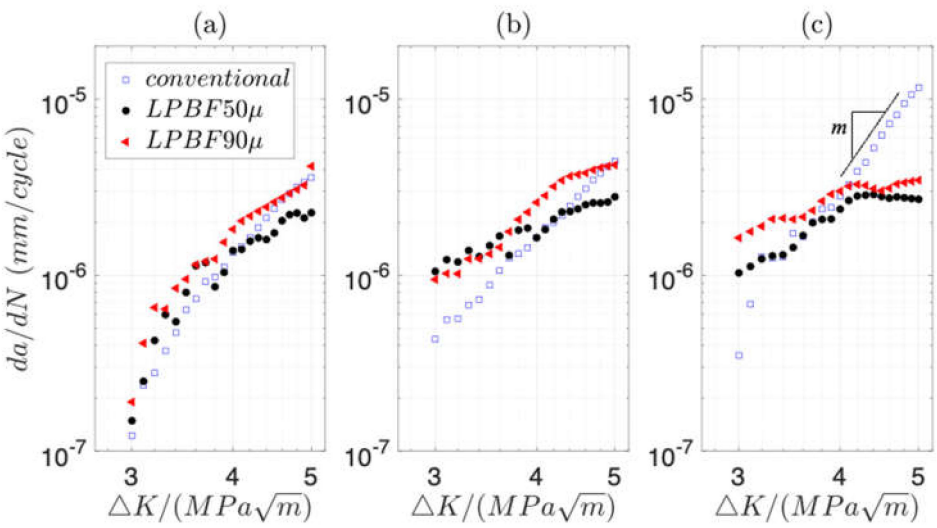

Figure 6. Fatigue crack growth kinetics of 316L SS at different corrosion fatigue parameters for conventional (labeled as conventional) and two LPBF samples at H = 90 µm and H = 50 µm (la-beled as LPBF90µ and LPBF50µ, respectively) at R = 0.833 in (**a**) air, (**b**) 3.5 wt.% NaCl solution at 20 Hz and (**c**) 3.5 wt.% NaCl solution at 2 Hz.

These tests were also conducted under R = 0.833 (Figure 6). The increase in crack growth rate of the conventional sample was pronounced, with longer exposure to solution as the crack propagated. In contrast, the increase in growth per cycle of LPBF samples in solution was very limited. The growth was even suppressed at a higher crack length. This indicates that the LPBF samples may possess strong anti-corrosion properties, and newly formed slip planes during cyclic loading passivate quickly. Overall, at the reduced hatch spacing condition (H = 50 µm), the crack growth rate was lower than that at H = 90 µm. A fit to the data using Paris' law $da/dN = C(\Delta K)^m$ was conducted for this condition and the extracted parameter m, which is the slope of the log(da/dN)~log(ΔK) plot, is listed in Table 4.

Fracture morphology shows that the crack branches propagate predominately in an intragranular mode (Figure 7). This intragranular cracking mode is very likely related to the absence of chemical segregation and intergranular precipitates identified in the materials characterization (Supplementary Materials). Therefore, the intragranular cracking is possi-

bly due to the homogeneous chemical and mechanical properties. Our current and future work includes corrosion fatigue testing of heat-treated AM samples, where the chemical segregation and precipitations around dislocation subgrains and grain boundaries have been found. In this case, intergranular corrosion would likely occur and possible difference in crack propagation mode (inter- or intra- granular) would be identified. In addition, the corrosion fatigue test would be conducted in the passivity and pitting corrosion regime through an applied electrochemical potential under cyclic loading. The sample in passivity is assumed to be mainly dominated by mechanical factor. The crack propagation mode under the different conditions would also be analyzed.

Table 4. Summary of the (**a**) HCF and (**b**) FCP results. For the HCF test, "X" represents that no test has been conducted for that condition. All the tests were stopped at the 10^7 cycle. If no failure occured, the endurance limit was assumed to be reached.

(a)	**Number of Life Cycle to Failure**			
Maximum Stress, MPa	Conventional		LPBF50μ	
	air	3.5 wt.% NaCl	air	3.5 wt.% NaCl
600	1.01×10^5	4.88×10^4	5.37×10^4	4.68×10^4
550	1.65×10^5	X	1.28×10^5	X
500	2.41×10^5	8.59×10^4	6.01×10^4	1.18×10^5
475	1.00×10^7	X	1.00×10^7	1.87×10^5
450	X	X	X	1.00×10^7
400	X	2.33×10^5	X	X
350	X	5.91×10^5	X	X
325	X	1.00×10^7	X	X

(b)	***m*, Fatigue Crack Propagation at R = 0.833**				
	Conventional			LPBF50μ	
Air	3.5 wt.% NaCl, 20 Hz	3.5 wt.% NaCl, 2 Hz	air	3.5 wt.% NaCl, 20 Hz	3.5 wt.% NaCl, 2 Hz
6.02	4.54	5.84	4.43	1.88	2.16

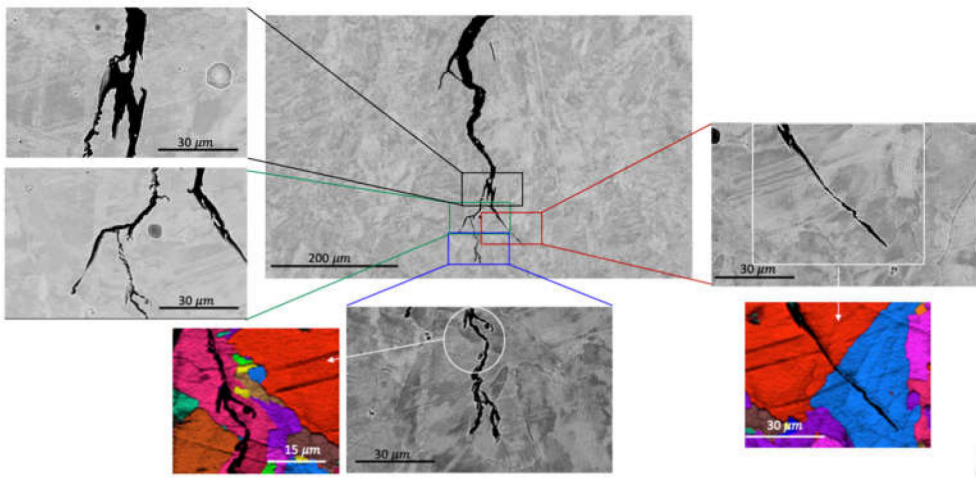

Figure 7. SEM and EBSD images of the fracture morphology showing that the crack predominately propagates in an intragranular manner of the LPBF 316L SS in 3.5 wt.% NaCl solution.

4. Discussion

In high cycle fatigue, the crack initiation typically dominates fatigue life, and thus determining where and how cracks initiate is critical to understand and control the fatigue life. However, in the corrosive environment it is very challenging to identify the exact microscopic defect/feature that leads to the initiation of the crack, which is often the

corroded site. Nevertheless, it can be deduced from the HCF tests that pitting forms faster in conventional than in LPBF samples.

Therefore, the presence of porosity, which may play a role in air fatigue, does not necessarily facilitate crack initiation in the corrosive environment, i.e., the pitting formation. This is also supported by the electrochemical corrosion measurements as shown in Figure 1a–c, where the pitting corrosion resistance of the LPBF sample is much higher than that of the conventional one. Furthermore, sample 7 (P = 195 V, V = 1408 mm/s) which contains a substantial number of pores, also demonstrated a pitting potential of around 641 mV, even higher than some dense samples (Figure 1d). This is consistent with the finding [10] that the critical pitting potential was not directly related to the amount and size of pores in 316L in the range of 0.01% to 0.4% porosity. Therefore, it is evidenced that the low degree of porosity does not deteriorate corrosion fatigue properties by facilitating crack initiation in the corrosive environment. The mestable pitting events increased during the passive domain, again consistent with the findings in [10].

In the FCP test, it was found that the growth rate in AM alloy became steadier, rather than accelerated, as the crack propagated in the corrosive environment, in contrast to their conventional counterpart. Crack propagation is typically related to the formation of persistent slip bands/steps. According to the passive film rupture and transient anodic dissolution mechanism [25], the protective passive film is likely to be disrupted during the cyclic loading through its interaction with slip bands. The passivation/repassivation of the disrupted passive film can strongly affect the crack propagation [26,27]. Thus, the slower crack growth rate of AM alloys in solutions indicates their enhanced passivation/repassivation properties. This was also confirmed using the CP test (Figure 2). It is worth mentioning that the charge transfer resistance of the passive film, which indicates its protectivity, was extracted through the electrochemical impedance spectroscopy, yet no significance differences were found for the differently processed 316L SS (Figure S4 and Table S2 in Supplementary Material).

Other than porosity, critical microstructural features also include precipitates or chemical segregation. However, SEM and transmission electron microscopic (TEM) analysis did not detect their existence (Figure S3 Supplementary Material). The enhanced corrosion and corrosion fatigue properties are, thus, most likely attributed to the unique columnar and cellular subgrain dislocation network of LPBF samples (Figure 8a,b). It has been found that reduced grain size, and thus larger area of grain boundary, significantly improves the critical pitting potential [28,29]. When pitting starts to occur, the Cr concentration decreases locally, but this area can be replenished by enhanced Cr diffusion through the subgrain boundaries.

On the other hand, previous studies of severely deformed alloys (strain level >20%) have shown that corrosion behaviors in general deteriorate. The reduced corrosion resistance is very likely due to the high-level deformation which affects passive film characteristics and potential pitting of highly defective sites, even though the exact role of dislocations is not clear [28,30,31]. A rough estimate of the dislocation density formed in the as-printed parts gives a value of ~ 4×10^{14} m/m^3 for a cell size of 400 nm, and a value of ~ 1×10^{15} m/m^3 for a cell size of 200 nm [24]. A dislocation density of 5×10^{14} m/m^3 corresponds to a strain of around 2%. This small strain is less likely to deteriorate the passive film and promote pitting formation according to relevant studies. Therefore, the introduction of dislocation networks could enhance the corrosion resistance of LPBF 316L SS by improving the diffusivity of anti-corrosion elements before they start to deteriorate the corrosion property by acting as potential pitting sites.

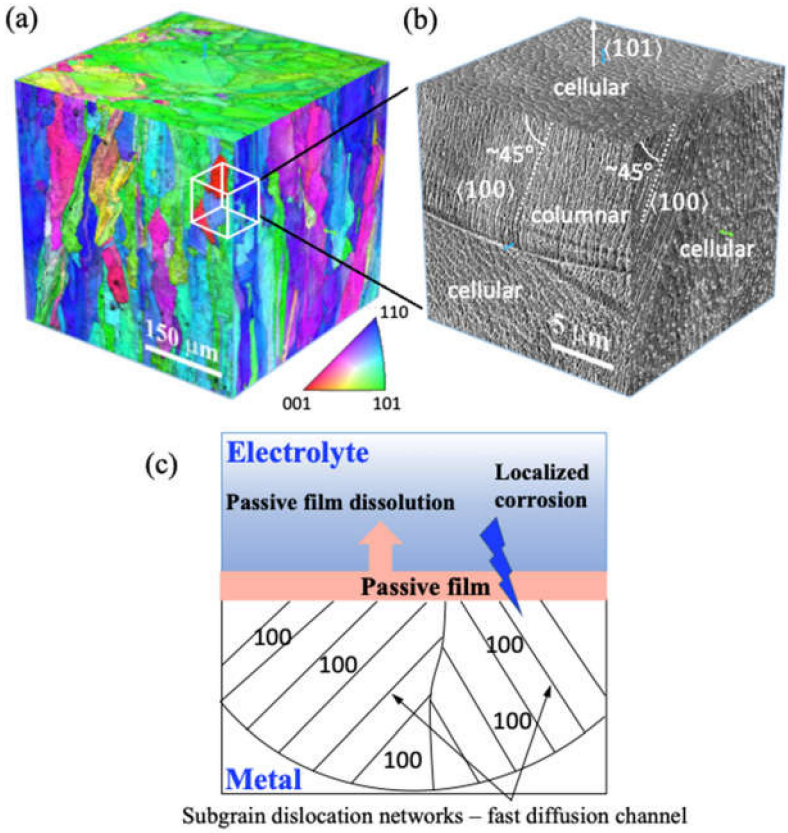

Figure 8. (**a**) Crystallographic planes and (**b**) orientation of the subgrain dislocation network on three coordinate planes, constructed from the EBSD-IPF and SEM images of the sample printed at P = 240 W, H = 50 μm (sample 6 in Table 1), (**c**) schematic of the role of dislocation cellular structure in promoting element diffusion.

5. Conclusions

1. The LPBF 316L SSs demonstrate, in general, improved corrosion resistance compared to conventionally manufactured 316L, as reflected by the increased pitting potential and higher repassivation potential.
2. While the endurance limit of high cycle fatigue testing is comparable between conventional and LPBF 316L in air, it is significantly higher for LPBF 316L than conventional ones in 3.5 wt.% NaCl solution.
3. The crack growth rate in air is, in general, higher in LPBF samples than in conventional ones. However, the growth rate in conventional 316L accelerates in 3.5 wt.% NaCl solution as the crack grows further. At reduced frequency in solution, the crack growth becomes retarded as the crack advances in the LPBF 316L.
4. The enhanced pitting corrosion resistance, higher endurance limit, and lower crack growth rate as the crack propagates in 3.5 wt.% NaCl solution of LPBF 316L compared to the conventional ones is likely to relate to the dislocation subgrain structure of the LPBF sample.

Supplementary Materials: The following are available online at https://www.mdpi.com/article/10.3390/met11071046/s1, Figure S1: Optical microscopy (OM) images of specimens printed with an increasing laser power from 150 W to 240 W at H = 90 μm (upper row) and H = 50 μm (middle row) and sample 7 (bottom row), Figure S2: (Upper panel) EBSD-IPF images and (bottom panel) kernel average misorientation (KAM) images generated with a step size of 0.15 μm and a threshold angle of 5° that indicate the grain orientation, measured on the XY plane at H = 50 μm with an increasing laser power from 150 W to 240 W, Figure S3: TEM images of subgrains showing (a) cellular and (b) columnar structure at the cross section, Figure S4: (a) Examples of (a) Bode plots for the passive

films of the LPBF-XY sample formed at the various passive potentials, and (b) the extracted interface transfer resistance from the EIS spectra, Table S1: The change in average grain size and KAM with printing parameters, Table S2: Characteristics of the passive film formed and tested at different potentials, obtained by fitting to the equivalent circuit.

Author Contributions: Conceptualization, Y.F. and J.S.; methodology, Y.F. and J.S.; investigation, B.G. and J.S.; resources, Y.F. and V.V.; data curation, B.G., Y.F. and J.S.; writing—original draft preparation, B.G. and Y.F.; writing—review and editing, B.G. and Y.F.; visualization, B.G. and J.S.; supervision, Y.F., J.S. and V.V.; project administration, Y.F.; funding acquisition, Y.F. All authors have read and agreed to the published version of the manuscript.

Funding: The APC was funded by University of Cincinnati startup fund.

Institutional Review Board Statement: Not applicable.

Informed Consent Statement: Not applicable.

Data Availability Statement: The data presented in this study are available in this article and its supplementary material.

Acknowledgments: We would like to express our gratitude to the Office of Naval Research [Award #: N00014-20-1-2284], which provided experimental support for this work. We would also like to extend our appreciation to the Advanced Materials Characterization Center (AMCC) at the University of Cincinnati for the use of the SEM and TEM in this research and the Ohio Center for Laser Shock Processing for Advanced Materials and Devices.

Conflicts of Interest: The authors declare no conflict of interest.

References

1. Petrousek, P.; Kvackaj, T.; Kocisko, R.; BIdulska, J.; Luptak, M.; Manfredi, D.; Grande, M.A.; Bidulsky, R. Influence of cryorolling on properties of L-PBF 316l stainless steel tested at 298K and 77K. *Acta Metall. Slovaca* **2019**, *25*, 283–290. [CrossRef]
2. Wang, Y.M.; Voisin, T.; McKeown, J.T.; Ye, J.; Calta, N.P.; Li, Z.; Zeng, Z.; Zhang, Y.; Chen, W.; Roehling, T.T.; et al. Additively manufactured hierarchical stainless steels with high strength and ductility. *Nat. Mater.* **2017**, *17*, 63. [CrossRef]
3. Ziętala, M.; Durejko, T.; Polański, M.; Kunce, I.; Płociński, T.; Zieliński, W.; Łazińska, M.; Stępniowski, W.; Czujko, T.; Kurzydłowski, K.J.; et al. The microstructure, mechanical properties and corrosion resistance of 316L stainless steel fabricated using laser engineered net shaping. *Mater. Sci. Eng. A* **2016**, *677*, 1–10. [CrossRef]
4. Ganesh, P.; Giri, R.; Kaul, R.; Sankar, P.R.; Tiwari, P.; Atulkar, A.; Porwal, R.K.; Dayal, R.K.; Kukreja, L.M. Studies on pitting corrosion and sensitization in laser rapid manufactured specimens of type 316L stainless steel. *Mater. Design* **2012**, *39*, 509–521. [CrossRef]
5. Chao, Q.; Cruz, V.; Thomas, S.; Birbilis, N.; Collins, P.; Taylor, A.; Hodgson, P.D.; Fabijanic, D. On the enhanced corrosion resistance of a selective laser melted austenitic stainless steel. *Scr. Mater.* **2017**, *141*, 94–98. [CrossRef]
6. Lodhi, M.J.K.; Deen, K.M.; Haider, W. Corrosion behavior of additively manufactured 316L stainless steel in acidic media. *Materialia* **2018**, *2*, 111–121. [CrossRef]
7. Andreatta, F.; Lanzutti, A.; Vaglio, E.; Totis, G.; Sortino, M.; Fedrizzi, L. Corrosion behaviour of 316L stainless steel manufactured by selective laser melting. *Mater. Corr.* **2019**, *70*, 1633–1645. [CrossRef]
8. Fazier, W.E. Metal Additive Manufacturing: A Review. *J. Mater. Eng. Perform.* **2014**, *23*, 1917–1928. [CrossRef]
9. Gu, D.; Shen, Y. Balling phenomena in direct laser sintering of stainless steel powder: Metallurgical mechanisms and control methods. *Mater. Design* **2009**, *30*, 2903–2910. [CrossRef]
10. Sander, G.; Thomas, S.; Cruz, V.; Jurg, M.; Birbilis, N.; Gao, X.; Brameld, M.; Hutchinson, C.R. On The Corrosion and Metastable Pitting Characteristics of 316L Stainless Steel Produced by Selective Laser Melting. *J. Electrochem. Soc.* **2017**, *164*, C250–C257. [CrossRef]
11. Kong, D.; Ni, X.; Dong, C.; Zhang, L.; Man, C.; Yao, J.; Xiao, K.; Li, X. Heat treatment effect on the microstructure and corrosion behavior of 316L stainless steel fabricated by selective laser melting for proton exchange membrane fuel cells. *Electrochim. Acta* **2018**, *276*, 293–303. [CrossRef]
12. Lou, X.; Othon, M.A.; Rebak, R.B. Oxide inclusions in laser additive manufactured stainless steel and their effects on impact toughness and stress corrosion cracking behavior. *J. Nucl. Mater.* **2018**, *499*, 182–190. [CrossRef]
13. Lou, X.; Othon, M.A.; Rebak, R.B. Corrosion fatigue crack growth of laser additively-manufactured 316L stainless steel in high temperature water. *Corros. Sci.* **2017**, *127*, 120–130. [CrossRef]
14. Lou, X.; Song, M.; Emigh, P.W.; Othon, M.A.; Andresen, P.L. On the stress corrosion crack growth behaviour in high temperature water of 316L stainless steel made by laser powder bed fusion additive manufacturing. *Corros. Sci.* **2017**, *128*, 140–153. [CrossRef]

15. Sun, S.-H.; Ishimoto, T.; Hagihara, K.; Tsutsumi, Y.; Hanawa, T.; Nakano, T. Excellent mechanical and corrosion properties of austenitic stainless steel with a unique crystallographic lamellar microstructure via selective laser melting. *Scr. Mater.* **2019**, *159*, 89–93. [CrossRef]
16. Cabrini, M.; Lorenzi, S.; Pastore, T.; Pellegrini, S.; Pavese, M.; Fino, P.; Ambrosio, E.P.; Calignano, F.; Manfredi, D. Corrosion resistance of direct metal laser sintering AlSiMg alloy. *Surf. Interface Anal.* **2016**, *48*, 818–826. [CrossRef]
17. Trelewics, J.; Halada, G.; Donaldson, O.; Manogharan, G. Microstructure and corrosion resistance of laser additively manufactured 316L stainless steel. *JOM* **2016**, *68*, 850–859. [CrossRef]
18. Cruz, V.; Chao, Q.; Birbilis, N.; Fabijanic, D.; Hodgson, P.D.; Thomas, S. Electrochemical studies on the effect of residual stress on the corrosion of 316L manufactured by selective laser melting. *Corros. Sci.* **2019**, *164*, 108314. [CrossRef]
19. Hemmasian Ettefagh, A.; Guo, S. Electrochemical behavior of AISI316L stainless steel parts produced by laser-based powder bed fusion process and the effect of post annealing process. *Addit. Manuf.* **2018**, *22*, 153–156. [CrossRef]
20. Salman, O.O.; Gammer, C.; Chaubey, A.K.; Eckert, J.; Scudino, S. Effect of heat treatment on microstructure and mechanical properties of 316L steel synthesized by selective laser melting. *Mater. Sci. Eng. A* **2019**, *748*, 205–212. [CrossRef]
21. Yusuf, S.M.; Gao, N. Influence of energy density on metallurgy and properties in metal additive manufacturing. *Mater. Sci. Technol.* **2017**, *33*, 1269–1289. [CrossRef]
22. Kluczyński, J.; Śnieżek, L.; Grzelak, K.; Mierzyński, J. The Influence of Exposure Energy Density on Porosity and Microhardness of the SLM Additive Manufactured Elements. *Materials* **2018**, *11*, 2304. [CrossRef] [PubMed]
23. Johnson, H.H. Calibrating the Electric Potential Method for Studying Slow Crack Growth. *ASTM Mater. Res. Stand.* **1965**, *5*, 442–445.
24. Gorsse, S.; Hutchinson, C.; Gouné, M.; Banerjee, R. Additive manufacturing of metals: A brief review of the characteristic microstructures and properties of steels, Ti-6Al-4V and high-entropy alloys. *Sci. Technol. Adv. Mater.* **2017**, *18*, 584–610. [CrossRef] [PubMed]
25. Ford, F.P. *Environment Induced Cracking of Metals*; Gangloff, R.P., Ives, M.B., Eds.; National Association of Corrosion Engineers: Houston, TX, USA, 1990; pp. 139–166.
26. Sieradzki, K.; Newman, R.C. Brittle behavior of ductile metals during stress-corrosion cracking. *Philos. Mag. A* **1985**, *51*, 95–132. [CrossRef]
27. Edeleanu, C.; Forty, A.J. Some observations on the stress-corrosion cracking of α-brass and similar alloys. *Philos. Mag. J. Theor. Exp. Appl. Phys.* **1960**, *5*, 1029–1040. [CrossRef]
28. Balusamy, T.; Kumar, S.; Sankara Narayanan, T.S.N. Effect of surface nanocrystallization on the corrosion behaviour of AISI 409 stainless steel. *Corros. Sci.* **2010**, *52*, 3826–3834. [CrossRef]
29. Rifai, M.; Miyamoto, H.; Fujiwara, H. Effects of Strain Energy and Grain Size on Corrosion Resistance of Ultrafine Grained Fe-20%Cr Steels with Extremely low C and N Fabricated by ECAP. *Int. J. Corros.* **2015**, *2015*, 1–9. [CrossRef]
30. Srinivasan, N.; Kain, V.; Birbilis, N.; Kumar, B.S.; Gandhi, M.N.; Sivaprasad, P.V.; Chai, G.; Lodh, A.; Ahmedabadi, P.; Samajdar, I. Plastic deformation and corrosion in austenitic stainless steel: A novel approach through microtexture and infrared spectroscopy. *Corros. Sci.* **2016**, *111*, 404–413. [CrossRef]
31. Fu, Y.; Wu, X.; Han, E.-H.; Ke, W.; Yang, K.; Jiang, Z. Effects of cold work and sensitization treatment on the corrosion resistance of high nitrogen stainless steel in chloride solutions. *Electrochim. Acta* **2009**, *54*, 1618–1629. [CrossRef]